Laser micromachining as a metallization tool for microfluidic polymer stacks

2013 J. Micromech. Microeng. 23 035020

(http://iopscience.iop.org/0960-1317/23/3/035020)

J. Micromech. Microeng. **23** (2013) 035020 (10pp) doi:10.1088/0960-1317/23/3/035020

Laser micromachining as a metallization tool for microfluidic polymer stacks

T Brettschneider[1], **C Dorrer**[1], **D Czurratis**[1], **R Zengerle**[2] **and M Daub**[3]

[1] Robert Bosch GmbH, Robert-Bosch-Platz 1, D-70839 Gerlingen, Germany
[2] IMTEK—Department of Microsystems Engineering, University of Freiburg, D-79110 Freiburg, Germany
[3] Robert Bosch GmbH, Tübinger Straße 123, D-72703 Reutlingen, Germany

E-mail: thomas.brettschneider2@de.bosch.com

Received 16 October 2012, in final form 10 December 2012
Published 1 February 2013
Online at stacks.iop.org/JMM/23/035020

Abstract
A novel assembly approach for the integration of metal structures into polymeric microfluidic systems is described. The presented production process is completely based on a single solid-state laser source, which is used to incorporate metal foils into a polymeric multi-layer stack by laser bonding and ablation processes. Chemical reagents or glues are not required. The polymer stack contains a flexible membrane which can be used for realizing microfluidic valves and pumps. The metal-to-polymer bond was investigated for different metal foils and plasma treatments, yielding a maximum peel strength of $R_{ps} = 1.33\,\mathrm{N\,mm^{-1}}$. A minimum structure size of 10 μm was determined by 3D microscopy of the laser cut line. As an example application, two different metal foils were used in combination to micromachine a standardized type-T thermocouple on a polymer substrate. An additional laser process was developed which allows metal-to-metal welding in close vicinity to the polymer substrate. With this process step, the reliability of the electrical contact could be increased to survive at least 400 PCR temperature cycles at very low contact resistances.

(Some figures may appear in colour only in the online journal)

1. Introduction

In recent years, an enormous amount of work has been done to expand the technological basis of microfluidic systems. Several different microfluidic platforms were developed, e.g., pressure-driven or centrifugal systems. A microfluidic platform is preferably based on a single fabrication technology and provides a wide range of microfluidic unit functions such as valving, pumping or mixing of fluids [1]. The idea behind the concept of microfluidic platforms is that these unit functions can be easily combined to more complex fluidic procedures, e.g., diagnostic assays in a lab on chip (LoC) [2, 3].

Many microfluidic platforms are polymer-based since from these materials, layers with microfluidic structures can be produced in high volumes at low costs by mass-production technologies such as injection molding or hot embossing [4–6]. Starting from a single structured layer, microfluidic systems can, e.g., be realized by covering the microfluidic structures with an adhesive tape. Alternatively, combined with a suitable joining technique, platforms based on polymer multi-layer stacks provide a higher degree of design freedom as fluids can be routed in a third dimension. In particular, the incorporation of a flexible membrane as an intermediate layer adds unique functions like passive [7] or pneumatically actuated valving and pumping [8–10].

On purely polymer-based platforms, physical effects which can be exploited are limited to the mechanical and rheological properties of polymers and the respective fluids. Many microfluidic effects which designers would like to add to their toolboxes, however, go beyond this and require the integration of electrically conducting materials. Among others, microfluidic applications utilizing the properties of conductors comprise heating and temperature control [11, 12], electrical and electrochemical sensing [13–16], electroosmotic pumping [17, 18] and particle manipulation by electrical forces [19–21].

In the past, different metallization techniques were applied to microfluidic systems, for example, standard microsystems technologies such as sputtering, evaporation or electroplating [13, 14, 21, 15, 18, 22]. These techniques, however, require clean room and vacuum conditions and often contain process

steps with organic solvents, limiting their applicability to silicon- or glass-based microfluidics. Screen and inkjet printing of conductor tracks on polymers have the advantage of being additive techniques; however, the conductivity is normally based on electrical contact between metal particles after the evaporation of a liquid phase, which leads to higher resistances than for pure metals [23, 24]. Other techniques are based on injecting conductive liquid materials such as eutectic gallium–indium or mercury into microfluidic channels to form electrode structures [25, 26] or the incorporation of conducting polymer composites [27, 28].

Here, a novel assembly approach for polymer LoCs with integrated metal structures based on laser micromachining is presented. The approach incorporates metal foils into a polymer stack consisting of transparent polymer substrate layers, which may contain microfluidic structures, and a flexible absorbing polymer membrane. In contrast to existing technologies, all assembly processes required for the complete system, i.e. bonding and structuring of the metal foil, joining of the multi-layer polymer stack as well as metal-to-metal welding, are performed with a single base technology, requiring only one standard laser scanning source. Hence, without the need for a set of different machines, vacuum or clean room environment, consumable components or tooling, our approach has the advantage of low investment and maintenance costs combined with a high degree of design freedom. Additionally, no chemical substances such as etchants, developers or glues are required for the production process. The process is therefore compatible with various polymers and no residues are left behind which might disturb in biochemical assays performed subsequently in the fabricated structures.

In the first part of this work, the basic process flow is presented. Then, the metallization approach is evaluated regarding the process technology, i.e. the influence of laser parameters, surface roughness and plasma treatment on the peel strength of the polymer–metal bond between polycarbonate and copper. Furthermore, minimum structure sizes are estimated based on the geometry of the laser cut line. In the second part, an on-chip temperature sensor is presented, which is to our knowledge the first standardized (type-T) thermocouple completely micromachined on a polymer substrate featuring direct thermal contact to the target medium. Accuracy against a reference and reliability of micromachined thermocouples are evaluated.

2. Basic process flow

All samples for characterization experiments as well as the demonstrators were manufactured following a basic process flow consisting of several laser-based steps. The starting point for this generalized process flow is a stack consisting of a polymer substrate transparent for the laser wavelength, an absorbing flexible polymer membrane and a metal foil. While maintaining contact, the flexible membrane is heated and liquefied in selected areas by laser radiation (figure 1(*a*)). At the interface between polymer membrane and polymer substrate, this results in the interdiffusion of the adjacent

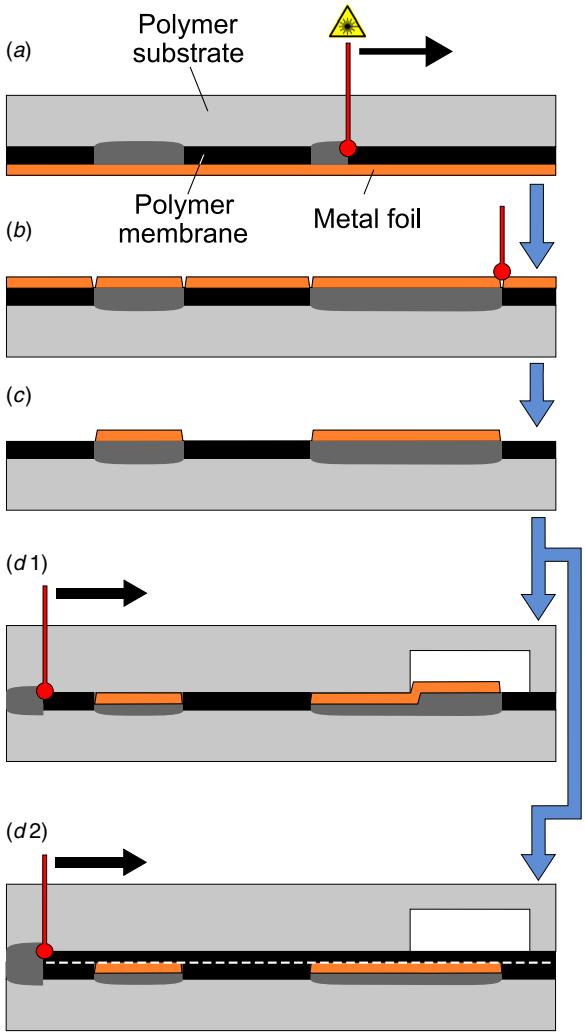

Figure 1. Basic process flow (not to scale). (*a*) Bonding of transparent polymer substrate, absorbing polymer membrane and metal foil by laser radiation. (*b*) Structuring of metal foil. (*c*) Removal of excess metal foil. (*d* 1) Laser welding of cover lid. Metal structures outside of microfluidic channels are pushed inside the elastic polymer membrane. (*d* 2) Alternatively, metal structures can be covered with another layer of polymer membrane.

materials and a stable bond after the solidification, as known from polymer laser welding processes [29]. During the same process step, the adhesion between polymer membrane and metal foil is achieved. Hence, the three-layer stack can be bonded within a single process step, while the scanning laser system allows to limit melting of the polymer membrane to areas selected for metallization. Moreover, since an unstructured metal sheet is used, no alignment against fluidic structures is necessary in this step.

In the next step (figure 1(*b*)), the metal layer is structured around the desired metal tracks via laser ablation after flipping of the assembled stack. The residual metal foil is not bonded to the polymer membrane and can be easily removed (figure 1(*c*)).

In a subsequent step, another substrate containing, e.g., microfluidic channels and cavities is attached by laser welding (figure 1(*d* 1)). In microfluidics, it is a well-known problem that tight sealing of conductor tracks against microfluidic structures is difficult to achieve due to the topography of the

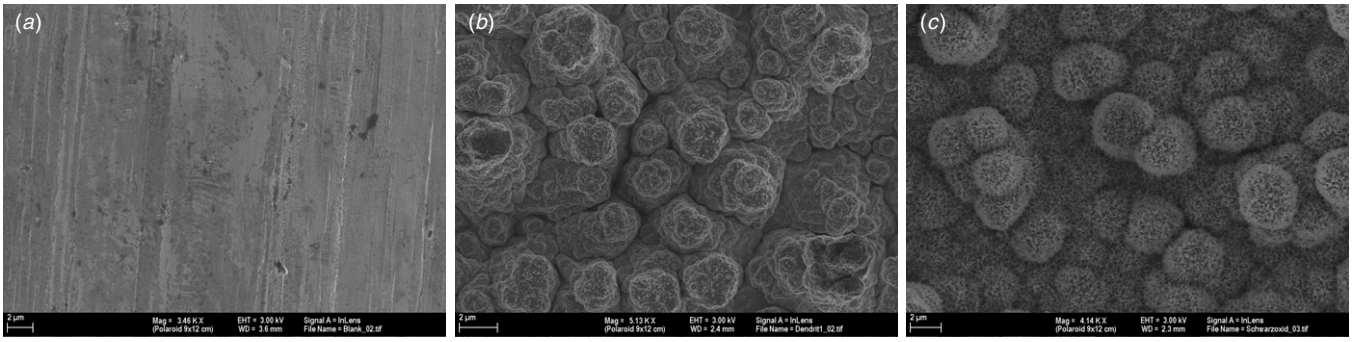

Figure 2. Scanning electron microscope (SEM) images to evaluate the surface roughness of different Cu foils. (*a*) Uncoated foil with a smooth surface. (*b*) Foils with electroplated dendrites. (*c*) Foil with black oxide treatment. The treated metal foils clearly show enhanced surface roughness.

metal layer [23]. In our approach, during laser welding in step (*d* 1), the metal foil outside of microfluidic channels is pushed into the polymer membrane. Moreover, every point of the conductor track edge close to the microfluidic cavity receives laser power during this step. As a result, the polymer membrane is molten in this region and closes any capillaries along the conductor track edge to provide tightness. Hence, tight sealing is achieved without any dispensing steps for glues or underfiller. Furthermore, the flexible polymer membrane can be used for realizing other microfluidic functions, e.g., valving or pumping, on the same substrate [8–10]. To further increase tightness, an additional layer of polymer membrane can be employed as depicted in figure 1(*d* 2). Depending on the application, the second layer can be kept close to shield the metal or open inside the microfluidic cavity by laser ablation to allow direct contact between metal and fluid.

3. Methods and materials

3.1. Sample fabrication

Channels and cavities on polymer substrates were milled from 1.5 mm thick injection molded polycarbonate slides (Makrolon 2605, Bayer Material Science). The flexible polymer membrane was based on a thermoplastic polyurethane with a thickness of 25 μm (Platilon U 4281 night black, Epurex Films GmbH). Four different metal foils were employed: uncoated copper (Cu) and copper–nickel (CuNi) foil (Cu-SE walzhart 10 μm, CuNi44 walzhart 12 μm, 55% Cu, 45% Ni, Carl Schlenk AG), black-oxide-treated Cu foil (Cu hot embossing foil 12 μm, Bolta Werke GmbH) and a Cu foil with an electroplated surface (JTCHTE 25 μm, Gould Electronics GmbH). Samples were cleaned with isopropanol and dried with nitrogen prior to laser bonding processes. A Nd:YAG laser system (LS9000, LS Laser Systems GmbH) with a wavelength of 1064 nm and a galvo mirror head was used to locally heat up the polymer membrane. During laser bonding, a force was maintained by pressing the stack between a glass and a metal base plate. For the attachment of metal foils, laser spot size and line distance were fixed to 100 μm with a laser pulse frequency of 4 kHz. Different energy inputs per unit length E_m were employed by keeping the laser spot velocity on the sample fixed to 34 mm s^{-1} and changing the laser power from 400 to 900 mW. To cover channels running on the backside, an adhesive tape (Polyolefin sealing foil, HJ Bioanalytik) was applied. For fluidic interfacing with silicone tubes, brass tubular rivets were glued (Endfest 300, UHU GmbH & Co. KG) onto the microfluidic chips. Oxygen plasma treatment of the polymer membrane was performed on a plasma system (Nano, Diener Electronic GmbH) with a power of 300 W for 300 s and an oxygen flow of 100 sccm.

3.2. Peel strength tests

Peel strength measurements were performed according to DIN EN 60249 with samples containing four metal tracks with a width of 4 mm and a length of 50 mm each. Samples were stored for three days at room temperature prior to testing. The force F was measured using a tensile testing machine (Zwicki 1120, Z2.5, Zwick GmbH) during peeling of the metal tracks with an angle of $90 \pm 4^\circ$ and a speed of 50 mm min^{-1}. The peel strength was defined as

$$R_\mathrm{ps} = \frac{\langle F \rangle}{b},$$

where $\langle F \rangle$ denotes the mean force F over a peel length of 45 mm and b denotes the width of the metal tracks.

3.3. 3D microscopy

Laser cut lines for different spot velocities v were structured on metallized polymer samples with a fixed pulse frequency of 4 kHz and a laser power of 3400 mW. An analysis of laser cut lines was conducted using a 3D microscope (Zeta 200, Zeta Instruments) with a field of view of $143 \times 190\,\mu\mathrm{m}^2$. Height raw data were analyzed using an automated Matlab routine to determine the edges of the cut line 5 μm below the surface and the mean width W for different laser parameters (cf figure 4(*b*)). The mean cross-sectional profile of the cut line was evaluated from 1024 single cross sections perpendicular to the cut line, yielding the depth D and bulge height B_h and width B_w.

3.4. Burst tests

To determine the burst pressure P_max of a typical microfluidic geometry, a circular cavity with a diameter of 4 mm was placed above a deposited conductor track of 500 μm in width and laser-welded against the polymer layers at a circular area

(45 mm^2) around the cavity. Samples were prepared with and without an additional polymer membrane as shown in figures 1(*d* 1) and (*d* 2). The burst pressure P_{max} was determined by placing the samples in a water bath and ramping the pneumatic pressure (3 kPa s^{-1}) until bubbles at the sample edges were formed.

3.5. Thermocouple reference measurements

For the reference measurement, a manufactured thermocouple was placed in a water bath together with a commercially welded type-T thermocouple (RS Components GmbH) as a reference. Thermocouples were carefully aligned to close vicinity without touching each other. During heating of the water bath with a hot plate, temperature signals were measured using a digital acquisition system (NI-cDAQ 9171 and NI-9211, National Instruments). Compensating wire of type-T (RS Components GmbH) was clamped to interfacing pads at the end of micromachined conductor tracks to connect the fabricated thermocouples to the acquisition system.

3.6. Resistivity and reliability tests

Samples for resistivity tests were electrically contacted by a frame containing contact spring probes. Four lanes, each consisting of 12 thermocouples, were connected in series and a constant current of 10 mA was applied. The voltage drop over the lanes was measured (NI-9215, National Instruments) and used to calculate the contact resistance R_{TC} of a single thermocouple. A thermocycler (Mastercycler Gradient, Eppendorf AG) was used to apply PCR temperature cycles for reliability tests (95°C; 60°C; 72°C; each for 30 s in one cycle).

4. Results and discussion

4.1. Characterization of the basic process

In this section, results of the laser bonding, ablation and burst pressure experiments are presented and discussed.

4.1.1. Peel strength. The adhesion between metal and polymer mainly depends on the surface energies of the materials involved. In general, the high difference in surface energy between metals and polymers leads to poor adhesion [30]. However, the surface properties of polymers can be modified to promote adhesion to metals, e.g., by plasma treatment [31–33] or ion bombardment [34, 35], which leads to new reactive binding sites or changes in polymer morphology. Another important parameter is given by the surface topography of the interfacing materials, which can promote surface adhesion due to an increase in surface area and mechanical interlocking. In this context, it is important to note that, for the metallization approach presented here, the polymer membrane in contact with the metal foil is completely molten, thereby adapting itself to the surface topography of the metal. Hence, in contrast to techniques such as sputtering or electroplating where it is the metal that adapts itself to the topography of the polymer, the adhesion in our case only depends on the topography of the metal and not on the roughness of the polymer surface.

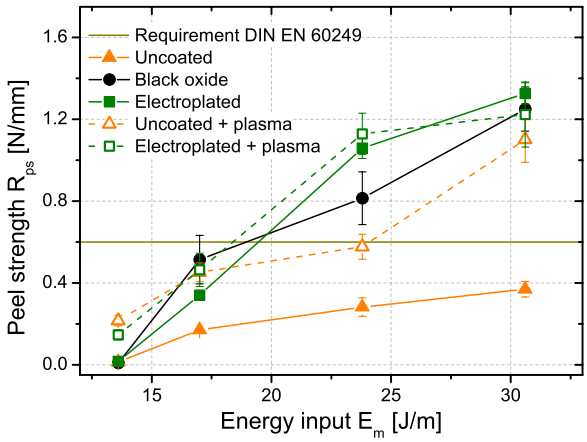

Figure 3. Peel strength R_{ps} over energy input E_m for different metal foils and polymer surface treatments. While the uncoated metal foil without polymer surface treatment (filled triangles) did not reach the DIN requirement for printed circuit boards, the peel strength was significantly increased by the surface treatment of the electroplated (closed squares) and black oxide foil (circles). Oxygen plasma treatment of the uncoated metal foil led to an increased peel strength comparable to the roughened metal foils (open triangles), while the enhancement effect for the electroplated foil was not significant (open squares).

To study the effect of roughness, foils with three types of roughness were included into the bonding experiments. Figure 2 clearly shows differences in the roughness between an uncoated Cu foil (figure 2(*a*)) and two metal foils for which the degree of surface roughness was increased by electroplating (figure 2(*b*)) and black oxide processing (figure 2(*c*)). While, under a scanning electron microscope (SEM), the uncoated metal foil hardly showed any anchor points for mechanical adhesion, the SEM images of the treated foils suggested that there may even be undercuts. It was expected that the peel strength R_{ps} would increase with surface roughness and also, as another parameter of interest, with the laser energy input E_m, as higher temperature should lead to a lower viscosity of the molten polymer and therefore to a better conformation to the metal topography.

Figure 3 shows the results for peel strength measurements, which were performed up to an energy input of $E_m = 31\,\mathrm{J\,m^{-1}}$. For higher energy inputs, laser radiation coupled into the interface between the polymer substrate and the glass plate from the sample holder and destroyed the sample surface. As expected, the peel strength R_{ps} increased for all metal foils with the higher energy input E_m. However, the slope was small for the untreated metal foil (closed triangles), which did not reach the requirement of $R_{ps} = 0.6\,\mathrm{N\,mm^{-1}}$ defined in DIN EN 60249 for printed circuit boards. Significantly higher peel strengths could be achieved with the electroplated (filled squares) and black oxide foil (circles), where this limit was reached at $E_m \approx 19\,\mathrm{J\,m^{-1}}$. At the maximum energy input, the electroplated foil yielded a peel strength of $R_{ps} = 1.33\,\mathrm{N\,mm^{-1}}$, which was more than twice the requirement from the DIN standard.

The effect of polymer surface modification was evaluated by oxygen plasma treatment of the polymer membrane prior to

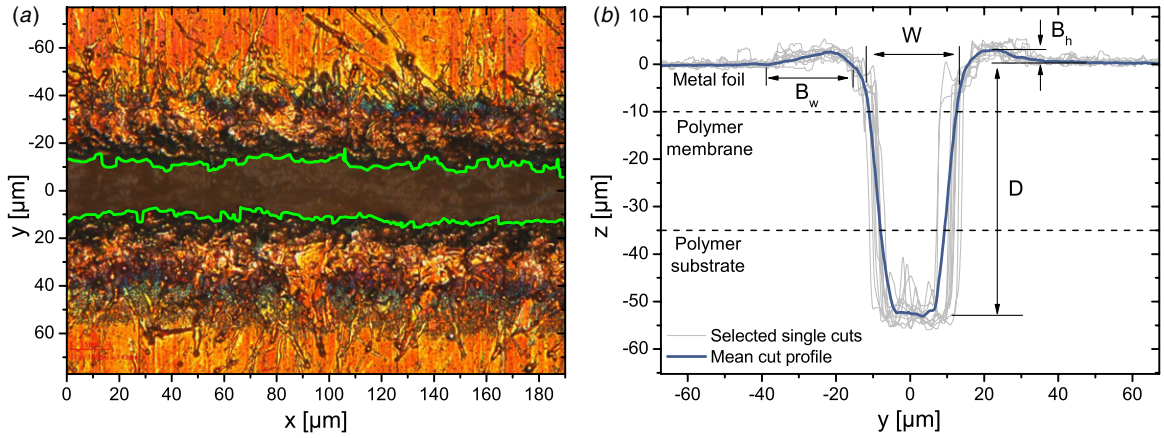

Figure 4. Typical laser cut line appearance and geometry. (*a*) Top view micrograph showing the ablated central track, the bulge formed from expelled material and the determined cut line edges (green line). (*b*) Exemplary single cross sections (thin lines) and cross section averaged over a complete sample (thick line) used to calculate depth D, width W, bulge height B_h and bulge width B_w.

laser bonding. As can be seen from figure 3, plasma treatment led to a significant increase in the peel strength R_{ps} in the case of the uncoated Cu foil (open triangles). For the electroplated foil, plasma treatment had a minor effect (open squares), which suggests that for this foil, mechanical adhesion dominated. Apart from that, for values below $R_{ps} = 1\,\mathrm{N\,mm^{-1}}$, all tested samples showed an adhesive failure between metal foil and polymer membrane, while above $R_{ps} = 1\,\mathrm{N\,mm^{-1}}$, mostly cohesive failure of the polymer membrane occurred. This indicates that such high peel strengths cannot be increased further by surface treatments, as the bulk properties of the polymer membrane limit the bond strength.

All experiments described in the following were performed with the blank Cu foil, using an energy input of $E_m = 24\,\mathrm{J\,m^{-1}}$ for the laser bonding process.

4.1.2. Cut line geometry. The minimum feature size of the deposited metal structures is mainly limited by the properties of the cut line, which is formed by laser ablation of the metal layer. During ablation, the energy of a laser pulse is partly reflected and partly absorbed by the metal, leading to a temperature increase above the boiling point and vaporization. In the vicinity of the illuminated area, thermal diffusion leads to the so-called heat affected zone, where the metal undergoes melting without vaporization [36, 37]. The dimensions of the heat affected zone can be estimated by the thermal diffusion length $l = 2\sqrt{\kappa\tau}$, where $\kappa = 111\,\mathrm{mm^2\,s^{-1}}$ denotes the thermal diffusivity of Cu [38] and τ denotes the pulse duration. With a pulse duration of $\tau = 230\,\mathrm{ns}$ of the employed IR laser, the size of the heat affected zone can be estimated to be in the order of 10 μm.

To reduce heat transfer and realize smaller structures, pico- or femtosecond UV laser sources are commonly employed for metal ablation [39–41]. However, most polymers are not transparent for UV radiation, which is a requirement for the metal foil attachment step. Hence, to show feasibility of the complete process with a single laser source, ablation experiments were performed on the same machine as a metal foil attachment.

Figure 4(*a*) shows exemplarily a top view image of a typical laser cut line for an uncoated metal foil attached to a polymer stack. It can clearly be seen that besides the vaporization of metal in the center of the cut line, a significant amount of material at the cut line edges was molten and expelled sideways, forming a bulge along the cutting track. To gain more insight into the geometry, 3D height data (figure 4(*b*)) were analyzed to find the edges of the cut line (green line) and the corresponding edge roughness R_c. Apart from that, the mean cross section perpendicular to the cut line (blue line in figure 4(*b*)) was determined from 1024 single cross sections, some of them exemplarily shown as gray lines. The mean cross section was used to calculate the bulge height B_h, bulge width B_w, depth D and width W.

Figure 5 shows the cut line analysis results for different spot velocities v. For the depth D, a maximum velocity of $v = 80\,\mathrm{mm\,s^{-1}}$ could be determined where the 10 μm thick metal foil was still completely cut through. Since a complete cutting of the metal foil is crucial for this process step, higher velocities with metal residues in the cut line were not further considered. With decreasing velocity v, more energy was deposited, leading to an increasing depth of the cut line up to $D = 49$ μm. At this velocity, the polymer membrane was removed completely, as well as 25 μm of the polymer substrate. However, for very low velocities below $v = 20\,\mathrm{mm\,s^{-1}}$, the high amount of absorbed energy led to a melting of the surrounding polymer and refilling the cut line track, which reduced the depth D. The results for the depth D show that, at higher velocities above $v \approx 60\,\mathrm{mm\,s^{-1}}$, it was possible to remove the metal foil with marginal damage to the underlying polymer substrate. Hence, the ablation process can be carried out without damage to structural features within the polymer substrate.

As shown in figure 5(*b*), the width W of the cut line decreased with higher velocities v. In general, it is expected that the width W mainly depends on the laser spot diameter which was constant during the experiments. Furthermore, as soon as the metal is removed, excess energy of the overlapping laser pulses was deposited in the polymer membrane and not in the metal foil, thereby preventing further ablation of metal.

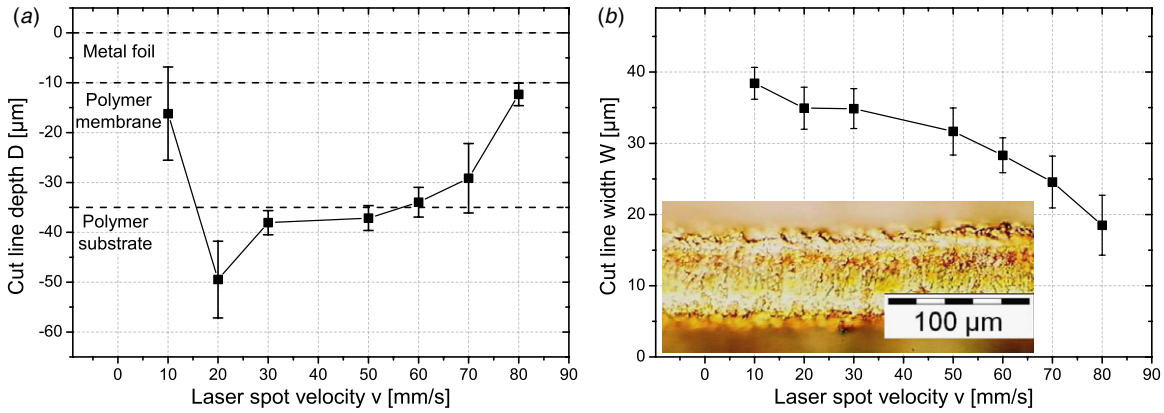

Figure 5. Dependence of the cut line geometry values for different laser spot velocities v. (*a*) The depth D decreased for increasing velocities v, reaching a value with minimum damage to the polymer membrane at $v = 80\,\mathrm{mm\,s^{-1}}$. For very low velocities v, the depth D decreased again due to refilling of the gap by a molten polymer. (*b*) The width W was reduced with increasing velocity v. *Inset*: part of conductor track with a width of 50 μm.

The decrease in width from $W = 38$ μm down to 19 μm with higher spot velocities can be attributed to the fact that in the outer regions of the Gaussian beam profile, the energy deposited in the material was not high enough for ablation at higher velocities. For the presented process, the minimum width $W = 19$ μm is an important parameter, as it defines the minimum isolation distance between metal structures.

While the bulge height decreased for higher spot velocities v from $B_\mathrm{h} = 4$ μm down to about 2 μm (not shown), no significant variation of the bulge width $B_\mathrm{w} = 22.3 \pm 3.3$ μm could be observed over all samples. This implies that the bulge width B_w is linked to the dimensions of the heat affected zone, which are independent of the varied laser parameters.

Minimum structure sizes of the presented metallization approach depend on the requirements of the application. If only a conductive track is needed, e.g., to transport electrical signals or energy, the deformation of the metal foil surface due to the bulge is irrelevant. Hence, the minimum structure size is limited by the roughness R_c of the cut line edges, which was determined as $R_\mathrm{c} = 5.0 \pm 2.9$ μm for all samples without any trend regarding laser parameters. This suggests that a minimum structure size of 10 μm can in principle be produced by this laser source, while conductor tracks down to 50 μm in width were realized in this study (inset in figure 5(*b*)).

If an undamaged surface area is required, e.g., for bonding with other conductors, the bulge height B_h and the width B_w have to be considered. In this case, a distance of at least 25 μm has to be added to every edge of the metal structure.

Although smaller structures could in principle be realized with a different laser source, the achieved accuracy is high enough for many polymer-based microfluidic applications, where structure sizes above 100 μm are usually sufficient for realizing, e.g., conductor tracks or electrodes.

4.1.3. Tightness of laser-welded polymer layers. To prove the fluidic tightness of the structures shown in figure 1, samples including a circular cavity above a metal track were fabricated according to section 3.4.

For the burst pressure of the samples without the additional polymer layer (figure 1(*d* 1)), a value of $P_\mathrm{max} = 289 \pm 24$ kPa was determined, which is significantly higher than typical pressures applied in microfluidic systems [1]. The samples with the additional polymer layer (figure 1(*d* 2)) withstood the maximum pressure available in our lab, resulting in a burst pressure of $P_\mathrm{max} > 780$ kPa.

This shows that for both geometries proposed in figures 1(*d* 1) and (*d* 2), the pressure resistance is suitable for microfluidic applications.

4.2. On-chip thermocouple

In the following section, the investigated basic process flow is used and extended to fabricate a thermocouple based on two different metal foils.

Many biochemical reactions required for LoC applications depend on precise temperature control, e.g., DNA hybridization [42] or PCR reactions [43], where temperature cycling is performed. Temperature monitoring is usually performed off-chip, e.g., by commercial temperature sensors thermally coupled against an outer surface of the system [44–46] or contactless measurement using IR radiation [47, 48]. For both techniques, temperature gradients within the LoC have to be accounted for when deducing the actual temperature of the fluid from the measured temperature. As this is associated with uncertainties and additionally requires new simulations and calibration experiments for any change in materials or geometries, live temperature monitoring at the point of interest, i.e. within a microfluidic channel or cavity, is highly desired. For such on-chip temperature measurements, thin-film techniques to apply Pt-based RTDs [11, 49, 12] or thermocouples [50–52] were presented; however, all these approaches use silicon or glass substrates and non-standard thermocouple materials. For polymer-based microfluidics, the integration of a commercial thermistor was presented [53]. Other approaches take an advantage of temperature-dependent properties of certain measurement fluids, e.g., measured by color change [54] or fluorescence [56].

4.2.1. Process flow. The fabrication of the on-chip thermocouple was based on two subsequent metallization

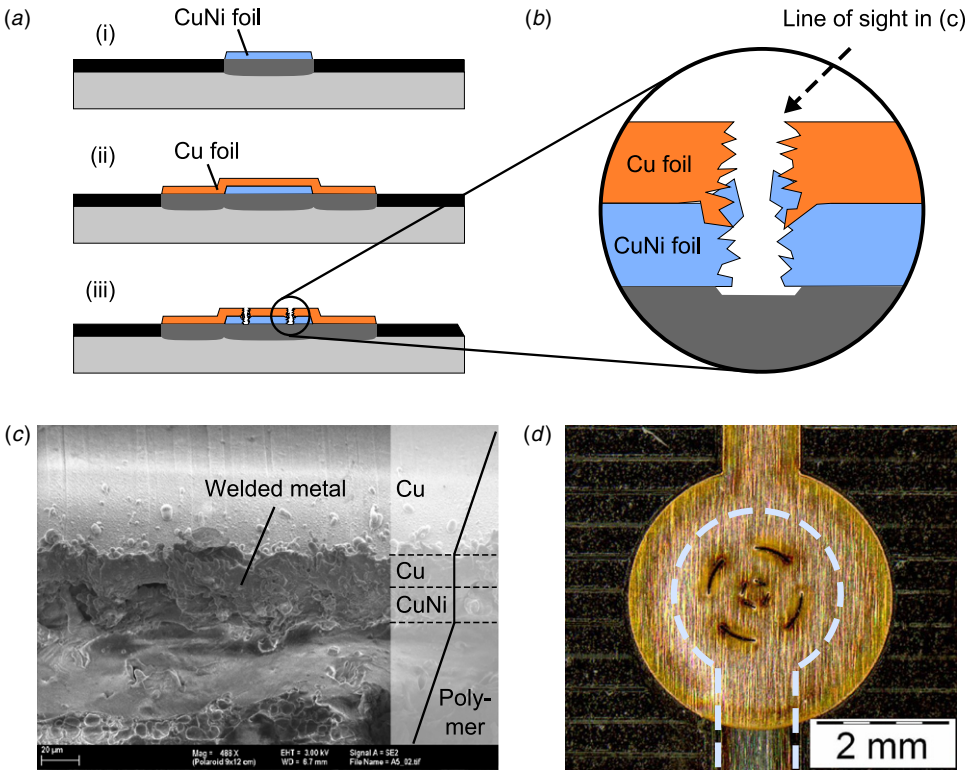

Figure 6. Laser micromachined thermocouple fabrication steps and sample images. (*a*) Process flow: (i) deposition of CuNi foil, (ii) deposition of overlapping Cu foil and (iii) metal welding by laser ablation. (*b*) Schematic cross section of the ablation cut line through both metal foils in detail. At the edges, the molten metal led to a welded joint between the metal foils. (*c*) SEM image showing a tilted view on the cut line. The metal foil edges were covered with the molten metal. (*d*) Top view micrograph on a fabricated thermocouple showing the Cu layer, CuNi layer (dashed line) and ablation pattern.

steps as described in section 2 and an additional ablation step (figure 6(*a*)). First, a CuNi conductor track was deposited (i), followed by a Cu layer overlapping the first CuNi layer (ii). The overlapping was needed to provide enough area for the bond between the Cu layer and the polymer. During laser welding, the Cu foil adapted to the underlying topography, thereby enclosing the CuNi conductor track. This ensured a tight contact between the two metal layers; however, it could be expected that an electrical contact based on two metal foils simply lying on top of each other is poor, especially due to oxide layers on the Cu foil.

During the production of commercial thermocouples, the wires are normally welded together, forming a mechanically stable and temperature-sensitive tip. Conventional welding of metals, however, cannot be employed in contact with the polymer substrate as the melting temperatures of Cu and CuNi (∼1200 °C) vastly exceed the pyrolysis temperatures of the involved polymers (∼200 °C). Here, a process was developed, where laser ablation through both metal foils was used to provide metal welding. During ablation, the major part of the absorbed energy is used to transfer the metal to the gas phase, resulting in a fairly low temperature budget for the polymer. However, as described in section 4.1.2, the high pulse length of the employed laser source leads to a heat affected zone. By ablating through the metal layers, both Cu and CuNi layers melted at the cut line edges, resulting in a weld line as indicated in figure 6(*b*). To prove this effect, the metal foils of a sample on one side of the cut line were removed, followed by the SEM inspection of the opposing sidewall at a tilted angle. As can be seen from figure 6(*c*), the cut line was completely covered with the molten metal. Hence, the effect of a heat affected zone, which is usually regarded as a disadvantage for high-resolution laser structuring, enabled the welding of metal foils in the first place.

Figure 6(*d*) shows a top view of a completely processed thermocouple. The Cu layer is visible, while the contours of the underlying CuNi layer are indicated by the dashed line. For the metal welding step, an ablation pattern consisting of several single lines was chosen.

Since especially PCR reactions are known to be inhibited by metal ions [55], another polymer membrane as described in figure 1(*d* 2) and section 4.1.3 can be employed as a shielding layer between metal and fluid. With a thickness of only 25 μm, the effect of this barrier layer on the temperature measurement is expected to be negligible.

4.2.2. Reference measurement. For the thermocouples in this study, care was taken in material choice to match the materials defined for type-T thermocouples, namely Cu and CuNi. To verify that the micromachined thermocouples matched the standard type-T relation between thermoelectric voltage and temperature, measurements in a heated water bath with a commercial thermocouple type-T as a reference were conducted. During the operation of microfluidic systems, the

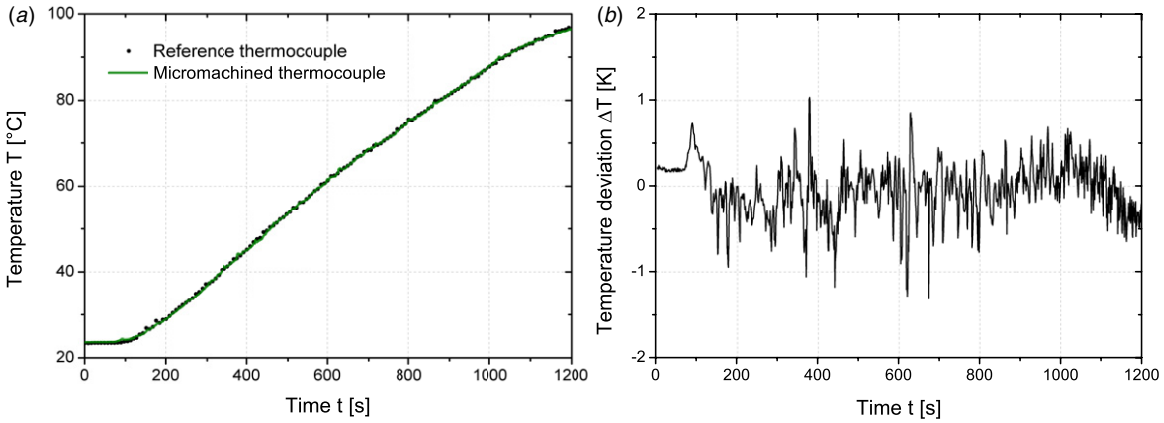

Figure 7. Reference measurements in a heated water bath. (*a*) Heating curve for micromachined (line) and commercial thermocouples (dots). (*b*) Temperature deviation ΔT between both thermocouples. With an overall standard deviation of $\sigma_{\Delta T} = 0.31$ K, a very good consistency could be achieved.

highest temperatures typically employed are defined by PCR denaturation steps, which may require temperatures up to $T = 98\,^{\circ}$C [43]. Figure 7 shows a heating curve (*a*) from room temperature to $T = 98\,^{\circ}$C for a micromachined (line) and reference thermocouple (dots) as well as temperature deviation ΔT between the thermocouples (*b*). As can be seen, the temperatures measured by the micromachined thermocouple were in very good agreement with the reference. The peak deviations up to $\Delta T = 1.3$ K can most likely be attributed to thermal convection during heating since the onset of fluctuations correlated with the beginning of the heating phase at $t \approx 70$ s. For the measured temperatures, an overall standard deviation of $\sigma_{\Delta T} = 0.31$ K could be determined, which lies within the tolerances of $\Delta T = 0.5$ K defined for class-1 type-T thermocouples in the standard IEC 60584-2.

4.2.3. Reliability tests. Although microfluidic systems are usually regarded as single-use devices, high demands can occur during the operation, e.g., due to temperature changes. In particular in heterogeneous systems like the presented polymer–metal stack, this can lead to high mechanical stress and reliability issues since the coefficient of thermal expansion (CTE) of polycarbonate is four times higher than the CTE of Cu $\alpha_{Cu} = 16.5 \times 10^{-6}\,K^{-1}$ [57]. For the thermocouples used in this study, the expansion of the polymer leads to a force between the metal layers, acting laterally on the contact area. Furthermore, higher temperatures promote the formation of oxides on the metal surfaces. As a result, during repeated temperature cycling, this could lead to a degradation of the electrical contact and failure of the thermocouple.

To investigate the reliability of the thermocouples, samples with 12 thermocouples connected in series were prepared and the electrical resistance R_{TC} per thermocouple was used as a parameter to describe the quality of the electrical contact between the metal layers, while typical PCR temperature cycles were performed between the measurements. To investigate the influence of the laser-based metal welding step, samples with and without the respective processing step were analyzed. As depicted in figure 8, already from the initial measurements, the resistances

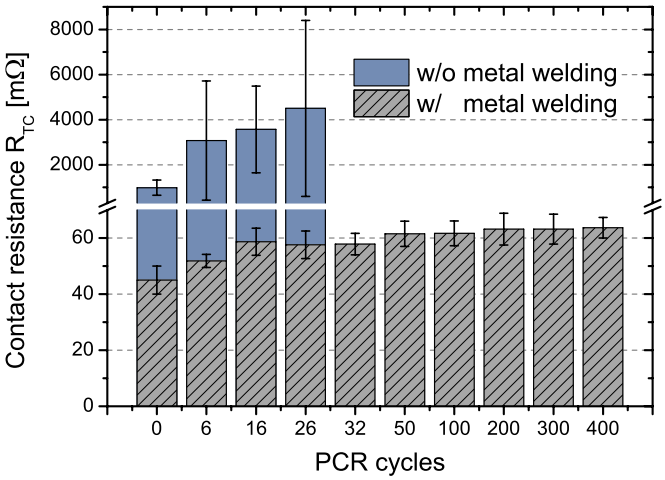

Figure 8. Thermocouple resistance R_{TC} after PCR cycle steps for samples with (shaded bars) and without metal welding steps (filled bars). Samples with metal welding showed a resistance 22 times smaller than the untreated samples. Untreated samples started to fail after 16 PCR cycles, while the welded samples were still functional after 400 cycles, with just a slight increase in resistance R_{TC}.

between thermocouples with (shaded bars) and without metal-to-metal welding (filled bars) differed by a factor of 22. During temperature cycling, the resistance R_{TC} and its variation clearly increased for the thermocouples without the welded interconnection, reaching a maximum value of $R_{TC} = 4500\,m\Omega$ after 26 cycles, while the electrical contact was lost on first samples after 16 cycles. After 26 cycles, none of the non-welded thermocouple lanes was functional. In contrast, all of the thermocouples which received the laser-based metal welding were still functional after 400 cycles, while the resistance increased only slightly to $R_{TC} = 64\,m\Omega$ with a low and nearly constant variation. Hence, the laser-based metal welding step had a decisive effect both on the absolute value of the thermocouple resistance R_{TC} and its variation. Moreover, it was an inevitable step to ensure reliability, as PCR cycles are typically repeated 30–40 times.

5. Conclusion

In this work, a novel fully laser-based approach for the metallization of polymer stacks for microfluidic applications was presented. For the metal-to-polymer bonding step, the peel strength could be significantly increased by plasma treatment of the polymer membrane and by using Cu foils with a roughened surface. With a peel strength clearly lying above the DIN requirement for printed circuit boards, this provides a sound basis for applications, e.g., requiring bonding steps to other conductors. The obtained minimum structure size of 10 μm was mainly limited by the size of the heat affected zone.

In the second part of this study, a standardized type-T thermocouple was micromachined on a polymer substrate. The process flow was extended by an additional laser-based step, where metal-to-metal welding was achieved by ablating through both metal foils. The electrical contact between the metal layers was stable for at least 400 typical PCR cycles which was ten times higher than the number of PCR cycles anticipated for a disposable microfluidic chip. Moreover, very good consistency of a micromachined thermocouple compared to a commercial reference with a standard deviation of $\sigma_{\Delta T} = 0.31$ K was observed.

The presented results show that all relevant process steps for applications requiring structure sizes down to 10 μm, high freedom of design and reliable interconnections could be carried out using a single solid-state laser source. In principle, all kinds of metals available as a foil can be integrated and interconnected to each other to form conductor tracks or electrodes, which could even be routed on different layers isolated by the polymer membrane. Furthermore, especially within lab-on-a-chip systems, the investigated thermoelectric contacts could also be used as Peltier elements for direct cooling and heating.

References

[1] Mark D, Haeberle S, Roth G, von Stetten F and Zengerle R 2010 Microfluidic lab-on-a-chip platforms: requirements, characteristics and applications *Chem. Soc. Rev.* **39** 1153–82

[2] Haeberle S and Zengerle R 2007 Microfluidic platforms for lab-on-a-chip applications *Lab Chip* **7** 1094–110

[3] Whitesides G M 2006 The origins and the future of microfluidics *Nature* **442** 368–73

[4] Becker H and Gaertner C 2008 Polymer microfabrication technologies for microfluidic systems *Anal. Bioanal. Chem.* **390** 89–111

[5] Boone T D, Fan Z H, Hooper H H, Ricco A J, Tan H and Willimas S J 2002 Peer reviewed: plastic advances microfluidic devices *Anal. Chem.* **74** 78–86

[6] Becker H and Locascio L E 2002 Polymer microfluidic devices *Talanta* **56** 267–87

[7] Jeon N L, Chiu D T, Wargo C J, Wu H, Choi I S, Anderson J R and Whitesides G M 2002 Microfluidics section: design and fabrication of integrated passive valves and pumps for flexible polymer 3-dimensional microfluidic systems *Biomed. Microdevices* **4** 117–21

[8] Rupp J *et al* 2012 Rapid microarray processing using a disposable hybridization chamber with an integrated micropump *Lab Chip* **12** 1384–8

[9] Araci I E and Quake S R 2012 Microfluidic very large scale integration (mVLSI) with integrated micromechanical valves *Lab Chip* **12** 2803–6

[10] Rupp J *et al* 2009 The way to high volume fabrication of lab-on-a-chip devices: a technological approach for polymer based microfluidic systems with integrated active valves and pumps *J. Microelectron. Electron. Packag.* **6** 198–204

[11] Chang Y H, Lee G B, Huang F C, Chen Y Y and Lin J L 2006 Integrated polymerase chain reaction chips utilizing digital microfluidics *Biomed. Microdevices* **8** 215–25

[12] Lao A I K, Lee T M H, Hsing I M and Ip N Y 2000 Precise temperature control of microfluidic chamber for gas and liquid phase reactions *Sensors Actuators* A **84** 11–17

[13] Ordeig O, Godino N, del Campo J, Muoz F X, Nikolajeff F and Nyholm L 2008 On-chip electric field driven electrochemical detection using a poly(dimethylsiloxane) microchannel with gold microband electrodes *Anal. Chem.* **80** 3622–32

[14] Becker H, Muehlberger H, Hoffmann W, Clemens T, Klemm R and Gaertner C 2008 Portable CE system with contactless conductivity detection in an injection molded polymer chip for on-site food analysis *Proc. SPIE* **6886** 68860C

[15] Gaertner C, Kirsch S, Anton B and Becker H 2007 Hybrid microfluidic systems: combining a polymer microfluidic toolbox with biosensors *Proc. SPIE* **6465** 64650F

[16] Wang J 2002 Electrochemical detection for microscale analytical systems: a review *Talanta* **56** 223–31

[17] Lazar I M and Karger B L 2002 Multiple open-channel electroosmotic pumping system for microfluidic sample handling *Anal. Chem.* **74** 6259–68

[18] McKnight E T, Culbertson C T, Jacobson S C and Ramsay J M 2001 Electroosmotically induced hydraulic pumping with integrated electrodes on microfluidic devices *Anal. Chem.* **73** 4045–9

[19] Voldman J 2006 Electrical forces for microscale cell manipulation *Annu. Rev. Biomed. Eng.* **8** 425–54

[20] Kang Y and Li D 2009 Electrokinetic motion of particles and cells in microchannels *Microfluid. Nanofluid.* **6** 431–60

[21] Wang L, Flanagan L and Lee A P 2007 Side-wall vertical electrodes for lateral field microfluidic applications *J. Microelectromech. Syst.* **16** 454–61

[22] Gavin P F and Ewing A G 1996 Continuous separations with microfabricated electrophoresis—electrochemical array detection *J. Am. Chem. Soc.* **118** 8932–6

[23] Becker H 2011 All I want for christmas... *Lab Chip* **11** 1571–3

[24] Vasudivan S and Zhiping W 2010 Fine line screen printed electrodes for polymer microfluidics *12th Electronics Packaging Technology Conf.* pp 89–93

[25] So J H and Dickey M D 2011 Inherently aligned microfluidic electrodes composed of liquid metal *Lab Chip* **11** 905–11

[26] Zhu X S, Gao C, Choi J W, Bishop P L and Ahn C H 2005 On-chip generated mercury microelectrode for heavy metal ion detection *Lab Chip* **5** 212–7

[27] Lewpiriyawong N, Yang C and Lam Y C 2010 Continuous sorting and separation of microparticles by size using AC dielectrophoresis in a PDMS microfluidic device with 3-D conducting PDMS composite electrodes *Electrophoresis* **31** 2622–31

[28] Gong X and Wen W 2009 Polydimethylsiloxane-based conducting composites and their applications in microfluidic chip fabrication *Biomicrofluidics* **3** 012007

[29] Duley W W and Mueller R E 1992 CO_2 laser welding of polymers *Polym. Eng. Sci.* **32** 582–5

[30] Kisin S, van der Varst P G T and de With G 2007 Adhesion and adhesion changes at the copper metal(acrylonitrilebutadienestyrene) polymer interface *Thin Solid Films* **515** 6853–9

[31] Kotal V, Svorik V, Slepika P, Sajdl P, Blahova O, Sutta P and Hnatowicz V 2007 Gold coating of poly(ethylene

terephthalate) modified by argon plasma *Plasma Process. Polym.* **4** 69–76
[32] Wang B, Eberhardt W and Kueck H 2005 Adhesion of PVD layers on liquid crystal polymer pretreated by oxygen-containing plasma *Vacuum* **79** 124–8
[33] Friedrich J F, Unger W E S, Lippitz A, Koprinarov I, Kuehn G, Weidner S and Vogel L 1999 Chemical reactions at polymer surfaces interacting with a gas plasma or with metal atoms their relevance to adhesion *Surf. Coat. Technol.* **116–119** 772–82
[34] Jung C H, Cho H W, Hwang I T, Choi J H, Nho Y C, Shin J S and Chang K H 2012 The effects of energetic ion irradiation on metal-to-polymer adhesion *Radiat. Phys. Chem.* **81** 919–22
[35] Bertrand P, Lambert P and Travaly Y 1997 Polymer metallization: low energy ion beam surface modification to improve adhesion *Nucl. Instrum. Methods* B **131** 71–78
[36] Baeuerle D 2011 *Laser Processing and Chemistry* (Berlin: Springer)
[37] Le Harzic R, Huot N, Audouard E, Jonin C, Laporte P, Valette S, Fraczkiewicz A and Fortunier R 2002 Comparison of heat-affected zones due to nanosecond and femtosecond laser pulses using transmission electronic microscopy *Appl. Phys. Lett.* **80** 3886–8
[38] Casalegno V, Vavassori P, Valle M, Ferraris M, Salvo M and Pintsuk G 2010 Measurement of thermal properties of a ceramic/metal joint by laser flash method *J. Nucl. Mater.* **407** 83–97
[39] Byskov-Nielsen J, Savolainen J M, Christensen M and Balling P 2010 Ultra-short pulse laser ablation of metals: threshold fluence, incubation coefficient and ablation rates *Appl. Phys.* A **101** 97–101
[40] Wynne A E and Stuart B C 2003 Rate dependence of short-pulse laser ablation of metals in air and vacuum *Appl. Phys.* A **76** 373–8
[41] Nolte S, Momma C, Jacobs H, Tünnermann A, Chichkov B N, Wellegehausen B and Welling H 1997 Ablation of metals by ultrashort laser pulses *J. Opt. Soc. Am.* B **14** 2716–22
[42] Sonntag F, Schmieder S, Danz N, Mertig M, Schilling N, Klotzbach U and Beyer E 2009 Novel lab-on-a-chip system for the label-free detection of DNA hybridization and protein–protein interaction by surface plasmon resonance (SPR) *Proc. SPIE* **7365** 73650Q
[43] Park S, Zhang Y, Lin S, Wang T H and Yang S 2011 Advances in microfluidic PCR for point-of-care infectious disease diagnostics *Biotechnol. Adv.* **29** 830–9
[44] Rahman M M 2000 Measurements of heat transfer in microchannel heat sinks *Int. Commun. Heat Mass* **27** 495–506
[45] Lagally E T, Simpson P C and Mathies R A 2000 Monolithic integrated microfluidic DNA amplification and capillary electrophoresis analysis system *Sensors Actuators* B **63** 138–46
[46] Peng X F, Hu H Y and Wang B X 1998 Flow boiling through v-shape microchannels *Exp. Heat Transfer* **11** 87–100
[47] Hetsroni G, Mosyak A, Pogrebnyak E and Rozenblit R 2011 Infrared temperature measurements in micro-channels and micro-fluid systems *Int. J. Therm. Sci.* **50** 853–68
[48] Roper M G, Easley C J, Legendre L A, Humphrey J A C and Landers J P 2007 Infrared temperature control system for a completely noncontact polymerase chain reaction in microfluidic chips *Anal. Chem.* **79** 1294–300
[49] Park H, Pak J J, Son S Y, Lim G and Song I 2003 Fabrication of a microchannel integrated with inner sensors and the analysis of its laminar flow characteristics *Sensors Actuators* A **103** 317–29
[50] Kwak B, Kim H, Cho J, Park J and Jung H 2008 Dual thermopile integrated microfluidic calorimeter for biochemical thermodynamics *Microfluid. Nanofluid.* **5** 255–62
[51] Lee W, Fon W, Axelrod B W and Roukes M L 2009 High-sensitivity microfluidic calorimeters for biological and chemical applications *Proc. Natl Acad. Sci. USA* **106** 15225–30
[52] Dijkstra M, Lammerink T S J, de Boer M J, Berenschot J W, Wiegerink R J and Elwenspoek M C 2008 Low-drift u-shaped thermopile flow sensor *IEEE Sensors* pp 66–69
[53] Burger J, Jaeger T, Gross A, Lastochkin A, Mark D, Roth G, von Stetten F, Zengerle R and Reindl L 2010 Direct on-disk wireless temperature measurement for centrifugal microfluidic platforms *Proc. 14th Int. Conf. on Miniaturized Systems for Chemistry and Life Sciences* pp 1502–4
[54] Ryu S, Yoo I, Song S, Yoon B and Kim J M 2009 A thermoresponsive fluorogenic conjugated polymer for a temperature sensor in microfluidic devices *J. Am. Chem. Soc.* **131** 3800–1
[55] Matheson C D, Marion E M, Hayter S, Esau N, Fratpietro R and Vernon K K 2009 Technical note: removal of metal ion inhibition encountered during DNA extraction and amplification of copper-preserved archaeological bone using size exclusion chromatography *Am. J. Phys. Anthropol.* **140** 384–91
[56] Samy R, Glawdel T and Ren C L 2008 Method for microfluidic whole-chip temperature measurement using thin-film poly(dimethylsiloxane)/rhodamine B *Anal. Chem.* **80** 369–75
[57] Haynes W M 2012 *CRC Handbook of Chemistry and Physics* (Boca Raton, FL: CRC Press)